water

MDPI

*Article*

# More about Persulfate-Assisted Ferrilanthanide-Mediated Photocatalysis of Textile Industry Dye Reactive Black 5: Surface Properties and Structural Assessment

**Idil Arslan-Alaton [1,*], Olga Koba-Ucun [1], Nazli Turkten [2], Isabella Natali Sora [3] and Miray Bekbolet [4]**

[1] Department of Environmental Engineering, School of Civil Engineering, Ayazaga Campus, Maslak, Istanbul 34469, Turkey
[2] Department of Chemistry, Faculty of Arts and Science, Kirsehir Ahi Evran University, Kirsehir 40100, Turkey
[3] INSTM and Department of Engineering and Applied Sciences, University of Bergamo, 24044 Dalmine, Italy
[4] Institute of Environmental Sciences, Bogazici University, Bebek, Istanbul 34342, Turkey
* Correspondence: arslanid@itu.edu.tr

**Abstract:** Color and organic matter removal from dyehouse effluent remains a challenging issue for the environmentalist and textile dyer. Until now, various treatment processes have been proposed with limited success. In this study, the textile dye and model industrial pollutant Reactive Black 5 (RB5; 20 mg/L) could be rapidly degraded by persulfate (PS)-enhanced photocatalytic treatment using a novel, home-made lanthanum iron oxide (LF; 0.5 g/L). LF-mediated heterogeneous photocatalysis was effective when the solution pH was kept below 4. The photocatalytic degradation of RB5 solution was enhanced in the presence of 0.6 and 1.2 mM PS. The dissolved organic carbon (DOC) content of the aqueous, hydrolyzed RB5 solution (initial DOC = 5.15 mg/L) was effectively reduced by LF/UV-A (LF = 0.5 g/L; 52–54% DOC removal after 150–180 min) and LF/PS/UV-A (LF = 0.5 g/L; 60–66% DOC removal after 120 min) treatments. LF photocatalyst could be reused in four consecutive cycles for complete color and partial DOC removals without significant deterioration of the treatment performance with the LF/PS/UV-A/pH 3 process. Instrumental analyses of LF's surface morphology/chemical composition and structural features via EDAX/SEM/Raman/FTIR/UV-vis/fluorescence spectroscopy indicated that LF remained practically intact throughout photocatalytic treatment, though slight changes/decreases in particle size/partial surface deformation and agglomeration coverage were observed, particularly during LF/PS/UV-A treatment. The presence of RB5 and its degradation products on the LF surface revealed that surface adsorption played a major role in LF-mediated photocatalysis. The Fe-content did not deviate appreciably from its original value after photocatalytic treatment.

**Keywords:** Reactive Black 5 (RB5) textile dye; persulfate-enhanced lanthanum–iron-oxide-mediated heterogeneous photocatalysis; color and organic carbon removals; photocatalyst reuse; spectroscopy; surface properties and chemical composition



**Citation:** Arslan-Alaton, I.; Koba-Ucun, O.; Turkten, N.; Sora, I.N.; Bekbolet, M. More about Persulfate-Assisted Ferrilanthanide-Mediated Photocatalysis of Textile Industry Dye Reactive Black 5: Surface Properties and Structural Assessment. *Water* **2023**, *15*, 906. https://doi.org/10.3390/w15050906

Academic Editor: Chih-Huang Weng

Received: 29 January 2023
Revised: 15 February 2023
Accepted: 22 February 2023
Published: 26 February 2023



## 1. Introduction

Textile industry wastewater is known for its complex and refractory nature, mainly because of the use of various dyes and dye auxiliary chemicals. Among the textile industry dyes, fiber-reactive dyes deserve special attention since they cannot be used after the dyeing process and end up in the spent reactive dyebath effluent in their hydrolyzed, unfixed form [1]. Commercial dyes including reactive dyes are intentionally designed to resist biological degradation, photolytic/photochemical, as well as thermal decomposition, rendering them difficult-to-treat industrial chemicals [1,2]. Hence, the concentration of spent (hydrolyzed, unfixed) reactive dyes can easily reach higher "mg/L" (in water: ppm) levels in receiving natural water bodies and up to 100 mg/L in spent, reactive dyebath effluent [2]. Several advanced treatment methods, such as adsorption, membrane operations, as well

as advanced chemical/photochemical/photocatalytic oxidation processes (abbreviated as AOPs; namely (photo)sonolysis, Fenton, Photo (ferrioxalate)-Fenton, semiconductor-mediated heterogeneous photocatalysis, (photo)catalytic ozonation, etc.) have already been studied for color and organic carbon removal from dyehouse effluent with promising results [3–5]. However, color removal from dyehouse effluent remains an unsolved treatment problem, particularly in developing countries where affordable, ecologically friendly and hence "sustainable" treatment is prioritized. In fact, for efficient color removal, mostly energy-intensive, advanced treatment processes have to be employed. In the last decade, the use of sulfate radical ($SO_4^{\bullet-}$)-mediated AOPs have attracted great interest, and persulfates (peroxydisulfate; peroxymonosulfate) have been activated by thermal, sonolytic, photolytic, and photocatalytic means, with great promise. $SO_4^{\bullet-}$ is known to eventually be more selective and effective in the treatment of several refractory organic pollutants found in water and wastewater [6,7]. In particular, the positive role of persulfates in heterogeneous photocatalysis has been explored and explained by a complex, multi-step free-radical-based mechanism [8]. Among the semiconductor materials, perovskite-type oxides with general-formula $ABO_3$ have received great attention because of their unique physicochemical properties [9,10]. Perovskite-structured lanthanum–iron oxide ($LaFeO_3$; abbreviated as LF herein) nanoparticles are commonly used for fuel cells, as well as magnetic and gas sensors [9–11]. In recent work, their photocatalytic activity under near-UV, visible, and solar light radiation has also been explored [12,13]. LF has shown great potential for the degradation and inactivation of various complex, organic pollutants, e.g., humic acids and microorganisms [14–16]. More recently, Koba-Ucun et al. [17] investigated the potential of a home-made LF photocatalyst in the degradation of the textile diazo dye Reactive Black 5 (RB5) that was selected as the model refractory industrial pollutant under UV-A light irradiation. In that study, the effect of peroxydisulfate (PS) on LF/UV-A treatment was explored for the first time. Their work focused on process optimization (effect of LF concentration and pH), the effect of PS addition, elucidation of color and dissolved organic carbon (DOC)-removal kinetics, as well as the reuse potential of the LF photocatalyst. LF/PS/UV-A and LF/UV-A treatments were also applied to real tap water and treated urban sewage effluent samples to examine their DOC-removal performance [17]. The authors also studied Fe release to explain the role of PS in LF/PS/UV-A treatment for color and DOC removals from a hydrolyzed RB5 solution. However, more comprehensive research based on instrumental analytical methods would be necessary to explain the reaction mechanism, oxidation enhancement, and LF-reuse performance of the LF/UV-A and LF/PS/UV-A processes to gain a better insight into this photocatalytic treatment process before their real-scale application potential could be envisioned.

Considering the above-mentioned issues, the present study was planned as an extension of the above-mentioned previous work on the LF/UV-A and LF/PS/UV-A treatments of industrial pollutants. It aimed to explore the potential of a home-made LF photocatalyst in the degradation of the commercially important textile industry dye RB5, which was again selected as the model refractory industrial pollutant. In the first part of the present study, the treatment performance and reuse potential of LF in LF/UV-A and LF/PS/UV-A treatments were demonstrated. The treatment performance was followed by measuring changes in color and DOC, while the reuse potential was assessed by using the same LF photocatalyst in four consecutive cycles for color and DOC removals. In the second and major part of this work, changes in chemical composition and surface morphology before and after LF/UV-A and PS/UV-A treatments via EDAX/SEM/FTIR/RAMAN measurements were explored in detail. Experimental findings and instrumental analytical results were supported with spectroscopic measurements. The novelty of this work not only comes from the treatment approach, but also the extensive instrumental assessment of the surface properties and structural changes in the home-made photocatalyst.

## 2. Materials and Methods

### 2.1. Materials

Home-made LF with a particle size of 43 nm and a BET surface area of 13 $m^2/g$ was used in the photocatalytic experiments. The synthesis and characterization procedures were described elsewhere [14,18]. Aqueous RB5 was prepared as a 0.4 g/L RB5 stock solution in hot (60–70 °C) distilled water. In total, 4.0 g/L of 12 N NaOH was added into the hot stock solution to ensure complete hydrolysis of the fiber-reactive dye [19]. Prior to each run, the stock solution was adjusted to room temperature and diluted to 20 mg/L RB5 with distilled water, then its pH was adjusted to the desired value to mimic reactive dyehouse effluent from the washing and rinsing stages. All chemicals used in this study were analytical grade and purchased from Merck (Darmstadt, Germany).

### 2.2. Photocatalytic Experiments

Details of the photocatalytic reactor set-up were given elsewhere [19]. The total incident photon flux of the UV-A lamps $I_0$ was 0.5 W/L (irradiated surface area: 94.2 $cm^2$). Prior to all photocatalytic experiments, the pH of the hydrolyzed RB5 solution was adjusted with 1–6 N $H_2SO_4$. Thereafter, LF photocatalyst was added into the reaction solution and the slurry was stirred for 10–15 min in the dark in order to obtain an equilibrium adsorption condition, which has been established in previous work as the dark pre-equilibrium adsorption time period for LF [16]. Photocatalytic experiments were run with and without PS, which was added at two different concentrations (0.6 mM and 1.2 mM) considering previous related work and the stoichiometry of PS to the RB5 dye. Finally, the photocatalytic reaction was initiated in the presence of UV-A light for 90, 180, 210, and 240 min depending on the type and kinetics of the treatment system (either LF/UV-A or LF/PS/UV-A).

### 2.3. Multiple-Reuse Experiments

Multiple-reuse experiments were conducted under optimized LF (0.5 g/L)/UV-A (0.5 W/L; 180 min) and LF (0.5 g/L)/PS (0.6 mM)/UV-A (0.5 W/L; 90 min; pH 3) treatment conditions. For this purpose, the used LF photocatalyst was filtered through 0.22 µm Millipore filters and rinsed several times with distilled water. The rinsed LF was dried in an oven (Memmert UF55; Schwach, Germany) for 60 min at 105 °C and stored in a desiccator prior to use. The LF samples were used in 4 consecutive cycles after applying the above treatment procedure.

### 2.4. Substrate Characterization, Photocatalyst Composition, and Morphology

#### 2.4.1. UV-Vis and Fluorescence Spectroscopic Analyses

UV-vis absorption spectra were recorded using a Perkin Elmer Lambda 35 spectrophotometer. Synchronous-scan fluorescence spectra were acquired by an A Perkin Elmer LS 55 luminescence spectrometer equipped with a 150 W xenon arc lamp and a red-sensitive photomultiplier tube in the excitation wavelength range of 200–600 nm ($\Delta\lambda$ = 18 nm). EEM fluorescence contour plots were constructed based on the fluorescence data recorded in the excitation wavelength range of 200–500 nm with 10 nm steps and emission wavelength range of 200–600 nm with 0.5 nm steps. EEM fluorescence contour plots were plotted as fluorescence intensity with respect to emission and excitation wavelengths by using Matlab 2013a.

#### 2.4.2. SEM/EDAX Analyses

Scanning electron microscopy (SEM) was complemented with ESEM-FEG/EDAX Philips XL-30 instrument operated at 20 kV. For SEM/EDAX analyses, samples were stuck on carbon tape and coated with a layer of platinum film.

#### 2.4.3. FTIR Analyses

FTIR measurements were carried out using a Thermo Scientific Nicolet 6700 spectrometer equipped with an attenuated total reflection accessory. The spectra were recorded in the frequency range of 4000–400 $cm^{-1}$ with a spectral resolution of 4.0 $cm^{-1}$.

#### 2.4.4. Raman Analyses

The Raman spectroscopy measurements were carried out by a Jobin Yvon LabRam confocal microscopy Raman spectrometer using laser excitation at 632.8 nm. The instrument was equipped with a charge-coupled device detector and a holographic notch filter. The He–Ne laser power applied on the samples was 20 mW. The spectra were recorded with a 1800 grooves/mm grating and a 200 µm entrance slit.

### *2.5. Other Analytical and Instrumental Procedures*

DOC was measured after centrifugation with a Shimadzu VPCN carbon analyzer (Kyoto, Japan) equipped with an autosampler. The pH measurements were performed with an Thermo Electron Orion 720 A pH-meter (Darmstadt, Germany).

## 3. Results and Discussion

### *3.1. Control (Baseline) Experiments*

Several control (UV-A-only, LF-only, PS-only, PS/UV-A) and LF/UV-A experiments were conducted as preliminary (control, baseline) experiments with 0.5 g/L LF (optimized concentration) and 20 mg/L hydrolyzed RB5 solution at varying pH values (3.0–11.5) for 120 min. During all control and LF/UV-A experiments run at pH > 4, color removal always remained below 10% except for PS/UV-A treatment, resulting in 83% color removal after 120 min treatment. Considering these findings, an acidic pH condition was required for the effective adsorption of the negatively charged RB5 (a benzene sulphonate salt and thus weak base) onto the LF surface (zero point of charge $pH_{zpc}$ = 8.9) and its subsequent photocatalytic degradation [14–16]. Hence, all photocatalytic treatment experiments were run at pH 3 and pH 4. However, SEM/EDAX, FTIR, and Raman analyses about changes in the structural features and chemical composition of LF before and during photocatalytic treatment of RB5 were performed at the entire studied pH range (3.0–11.5).

### *3.2. Photocatalytic Treatment Experiments*

Until now, several photocatalysts, including 2D and 3D metal-based nanomaterials, have been employed for textile dye degradation, as well as the removal of other micropollutants, with high treatment success [20–24]. In the present study, LF/UV-A and LF/UV-A baseline experiments with 0.6 mM and 1.2 mM initially added PS (indicated as "LF/PS/UV-A" herein) were conducted and comparatively evaluated at pH 3 and pH 4 for 90–210 min, depending on photocatalytic treatment efficiency and color removal rates. From the results shown in Figure 1, it was evident that over 90% color removal ($\lambda_{max}$ = 600 nm) was achieved after 60–90 min of LF/UV-A treatment of aqueous RB5 at pH 3. Preliminary dark RB5 adsorption was obtained as 13% and 20% at pH 3 and pH 4, respectively. For LF/UV-A treatment at pH 3, DOC removals reached 52–54% upon 90 min and fluctuated thereafter for 210–180 min, which we believed was due to the parallel increase in the reaction pH to >4, which was detrimental to RB5 removal with the LF/UV-A process. Color and DOC removals were appreciably enhanced in the presence of 0.6 mM and 1.2 mM PS as well. From previous related experimental work and our recent study [17], it was evident that PS had two functions in the treatment system; firstly, it acted as a conduction-band electron scavenger (Equation (2)), forming sulfate ($SO_4^{\bullet -}$) radicals that enhanced the oxidation of RB5 and its photocatalytic degradation products; contributing to the electron–hole charge separation on the LF surface (Equation (1)). Secondly, PS could react with the bulk and surface Fe (+II/+III) ions, initiating Fenton-like reactions that may also contribute to the photocatalytic oxidation rates (Equation (3)). From Figure 1 it is also apparent that color removal (a) was practically complete (>99%) in only 25–30 min for LF/PS/UV-A treatment,

accompanied with 60–66% DOC (b) removals after 120 min, which was also compared with 0.6 mM PS/UV-A treatment in the absence of LF resulting in only 83% color and negligible DOC removal (4%) thus emphasizing the expected enhancement in oxidation rates and efficiencies.

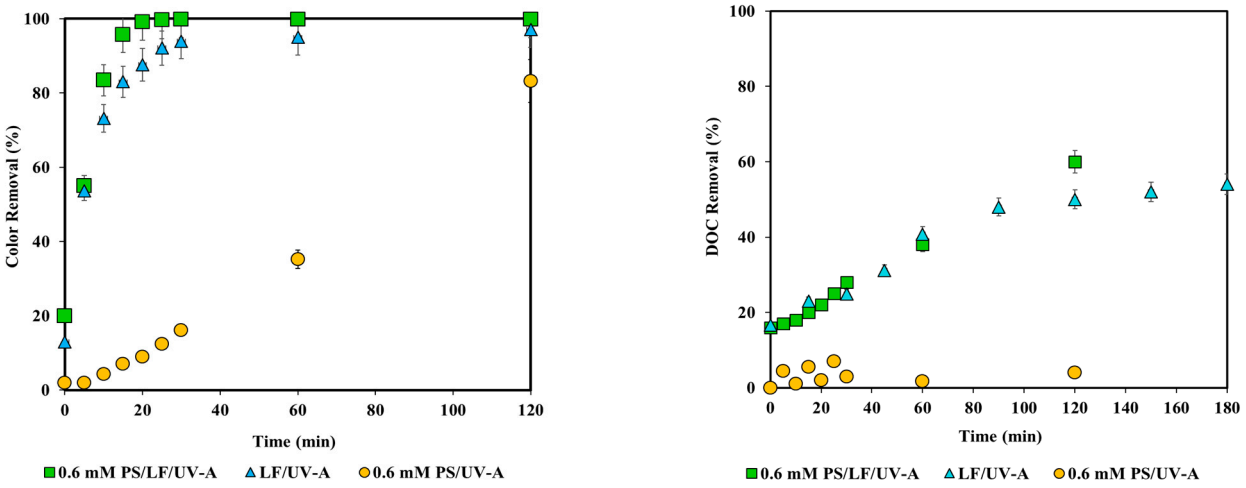


**Figure 1.** Color (peak absorbance) (**a**) and DOC (**b**) removal efficiencies obtained for LF/UV-A, LF/PS/UV-A, and PS/UV-A treatments. Experimental conditions: RB5 = 20 mg/L; pH = 3; LF = 0.5 g/L; PS = 0.6 mM; and $I_0$ = 0.5 W/L (UV-A).

The reaction equations that were mentioned above for (i) LF excitation, (ii) conduction-band electron scavenging by peroxydisulfate (PS), and the (iii) "Fenton-like process" between Fe(II) ions and PS are given below [7,8,17]:

$$LF + h\nu\ (E > E_{bg}) \rightarrow {e_{cb}}^- + {h_{\nu b}}^+ \quad (1)$$

$${e_{cb}}^- + {S_2O_8}^{2-} \rightarrow {SO_4}^{\bullet -} + {SO_4}^{2-} \quad (2)$$

$${Fe}^{2+} + {S_2O_8}^{2-} \rightarrow {Fe}^{3+} + {SO_4}^{\bullet -} + {SO_4}^{2-} \quad (3)$$

### *3.3. Photocatalyst Multiple-Reuse Experiments*

The reuse of (photo)catalyst materials is a critical area of investigation to complete the evaluation of the real-scale application potential of newly developed/home-made (photo)catalytic (nano)materials [7–10,17]. In the present study, LF was used in four consecutive cycles under optimized LF/UV-A and LF/PS/UV-A treatment conditions (0.5 g/L LF; 0.6 mM PS; pH 3; 0.5 W/L UV-A; and t = 210 min and t = 120 min, respectively) using hydrolyzed RB5 solutions (20 mg/L). The multiple reuse experiments indicated that there was no reduction in the performance throughout the treatment cycles involving LF/PS/UV-A/pH 3 (99% color, 61% DOC removal); however, the treatment performance worsened during LF/UV-A/pH 3 treatment (down to 90% color and 11% DOC removals). Figures 2 and 3 depict changes in color and DOC values for 180 min LF/UV-A (a) and 90 min LF/PS/UV-A (b) treatments after each of the four treatment cycles.

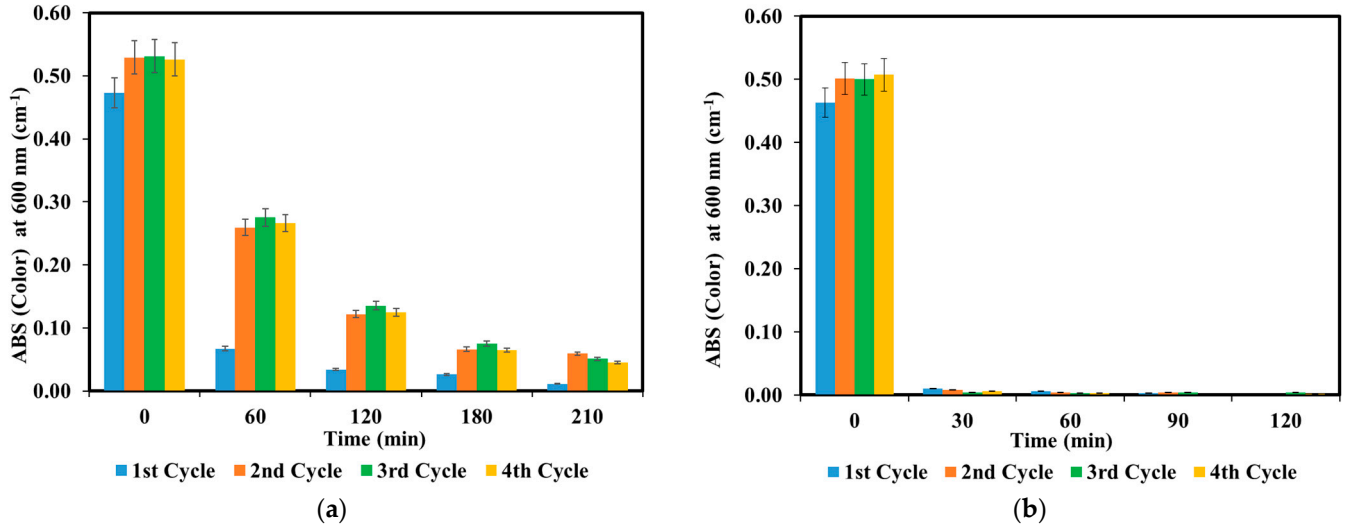


**Figure 2.** Changes in color (peak absorbance) values for LF/UV-A (**a**) and LF/PS/UV-A (**b**) treatments. Experimental conditions: RB5 = 20 mg/L; pH = 3; LF = 0.5 g/L; PS = 0.6 mM; $I_0$ = 0.5 W/L (UV-A); and t = 210 min for LF/UV-A and t = 120 min for LF/PS/UV-A treatment.

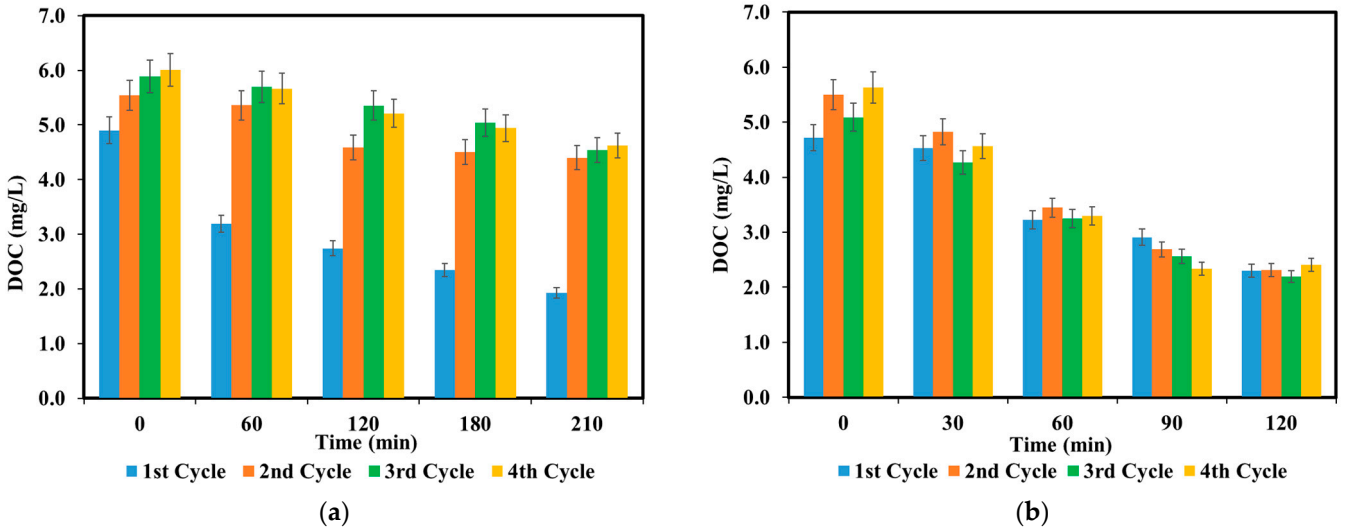


**Figure 3.** Changes in DOC values for LF/UV-A (**a**) and LF/PS/UV-A (**b**) treatments. Experimental conditions: RB5 = 20 mg/L; pH = 3; LF = 0.5 g/L; PS = 0.6 mM; $I_0$ = 0.5 W/L (UV-A); and t = 210 min for LF/UV-A and t = 120 min for LF/PS/UV-A treatment.

From the obtained color (Figure 2) and DOC (Figure 3) abatement profiles, it is obvious that the LF/PS/UV-A process outperformed the LF/UV-A process both in terms of RB5 (color) and DOC removals. Hence, LF/PS/UV-A could be preferably and safely applied without any reduction in the treatment performance of LF. Conclusively, LF/PS/UV-A treatment appeared to be the better, more suitable option for efficient and stable color and DOC removals from dyehouse effluent. In the next sections of the study, the surface properties, chemical composition, and morphology of the LF photocatalyst were studied to gain further insight into the application potential of LF for the treatment of complex parameters from industrial effluent.

### *3.4. Substrate Characterization, Photocatalyst Composition, and Morphology*

#### 3.4.1. UV-Vis and Fluorescence Spectroscopic Analyses of RB5 Degradation

The photocatalytic degradation of RB5 using a 0.5 g/L concentration of LF at pH 3 was monitored by UV-vis spectroscopy and displayed in Figure S1. Four peaks related to the benzene ring, vinyl sulfone, naphthalene ring, and azo double-bond regions of RB5 were observed. The maximum absorption peak ($\lambda_{max}$) in the visible region centered at $\lambda$ = 600 nm was assigned to the conjugated azo bonds (–N=N–) of the dye. The chromophore groups were responsible for the characteristic color of RB5. The intensity of this peak decreased gradually and disappeared after 240 min of irradiation, indicating that a complete decolorization was achieved. The three absorption peaks observed in the UV region of the spectrum located at $\lambda$ = 260 nm, $\lambda$ = 310 nm, and $\lambda$ = 392 nm were attributed to the benzene ring, vinyl sulfone, and naphthalene ring of RB5, respectively [25–27]. The naphthalene ring was more slowly degraded compared with the benzene ring and vinyl sulfone moieties of RB5, indicating much more stability in the photocatalytic system. However, upon the addition of PS, UV-vis spectral features were evidently lacking any significant absorbance variations at the specified wavelengths, displaying a steep increase at $\lambda$ < 250 nm. The synchronous scanning of fluorescence across a range of excitation and emission wavelengths can generate a profile spectrum, unlike the one-dimensional absorbance scanning of ultraviolet–visible wavelengths. Synchronous-scan fluorescence spectroscopic data displayed a major peak at $\lambda_{emis}$ = 350 nm and a minor peak at $\lambda_{emis}$ = 300 nm (Figure S2). The major peak at $\lambda_{emis}$ = 350 nm was accompanied with a shoulder peak at $\lambda_{emis}$ = 380 nm that diminished under early stages of treatment. The major fluorophores expressed a decreasing fluorescence intensity profile with respect to the increasing irradiation period, and both peaks converged upon the 120 min reaction period, indicating the co-presence of fluorophores related to the degradation products. The minor peak also displayed a decreasing profile with considerably lower fluorescence intensities. Furthermore, in the presence of PS, the synchronous-scan fluorescence features were apparently devoid of any fluorophores in accordance with UV-vis spectral features. On the other hand, fluorescence excitation–emission matrix spectroscopy is mainly used in the analysis of complex organic matrices. During the degradation process of dye molecules, the dye structure is generally easy to cleave, especially azo dyes, which could easily lead to substantial changes in the spectral response. In this respect, EEM fluorescence spectral profiles could bring further insight into structural diversities, demonstrating that LF/UV-A in the presence of PS (LF/PS/UV-A) proceeded much faster, which was related to the absence of any fluorophoric regions following 5–10 min, indicating that substrate removal is practically complete within minutes. The LF/UV-A treatment process on the other hand progressed slowly, and step-wise degradation could be followed by EEM fluorescence spectral features (Figure 4).

EEM fluorescence profiles were basically located in the regions of $\lambda_{exc}$ = 200–400 nm and $\lambda_{emis}$ = 325–425 nm with three compartments, the major of which was centered at $\lambda_{exc}/\lambda_{emis}$ = 225/350 nm. This region could be attributed to the presence of aromatic compounds composed of differing fluorophores that were either present in simple compounds or complex organic matrices [28,29]. Depending on the reaction mechanism, the removal of the parent compound and consecutive formation of new fluorophores could be visualized with diminished intensities in accordance with UV-vis and synchronous-scan fluorescence spectral features, as well as mineralization extents (Figures S1 and S2, respectively).

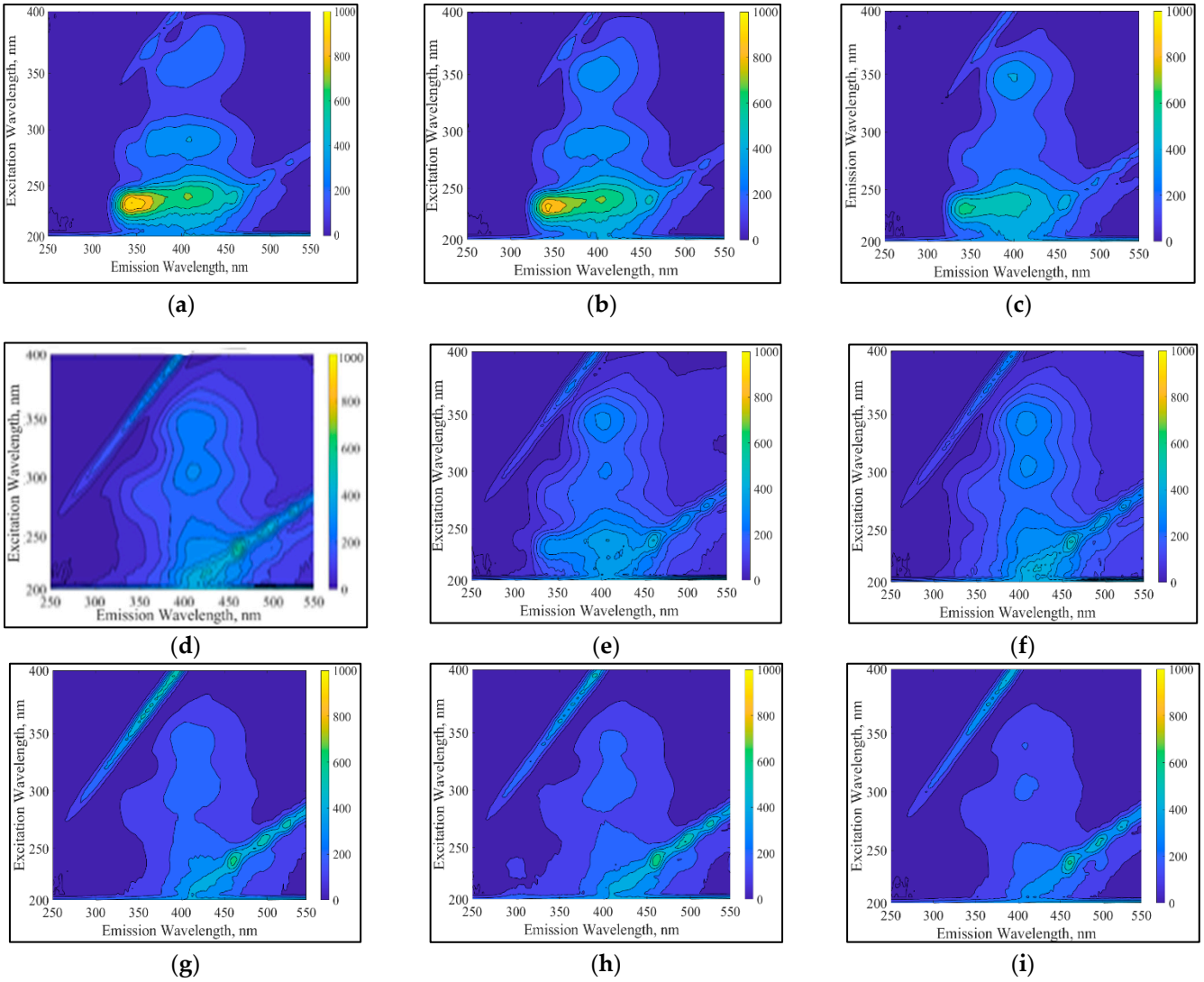


**Figure 4.** EEM fluorescence contour plots of RB5 at different irradiation times: (**a**) $t_{irr}$: 0 min; (**b**) $t_{irr}$: 5 min; (**c**) $t_{irr}$: 15 min; (**d**) $t_{irr}$: 30 min; (**e**) $t_{irr}$: 60 min; (**f**) $t_{irr}$: 120 min; (**g**) $t_{irr}$: 180 min; (**h**) $t_{irr}$: 210 min; (**i**) $t_{irr}$: 240 min. Experimental conditions: RB5 = 20 mg/L; pH = 3; LF = 0.5 g/L; $I_0$ = 0.5 W/L (UV-A).

### 3.4.2. SEM/EDAX Analyses

SEM analysis was performed at two different magnifications to examine the changes in the surface morphology of LF and RB-5 before and after photocatalytic at varying pH values (3.0–11.5). The effect of pH (3.0–11.5) on the LF/UV-A treatment performance of hydrolyzed RB5 has been reported in our previous work [17]. Moreover, EDAX analysis was evaluated for further confirmation of the product composition containing RB5 and LF obtained during photocatalytic treatment. In the first part of the SEM study, the effect of pH (3.0–11.5) on the photodegradation of RB5 was investigated. Figure S3a displays the image of sole LF consisting of various polyhedral-shaped particles and sizes. The particle sizes of LF varied from ~95 nm to ~170 nm. The EDAX spectrum indicated the existence of La, Fe, and O elements in the synthesized LF. SEM images in Figure S3b,c illustrate the morphology of LF particles during and after the photocatalytic degradation of RB5 at pH 3 and pH 4, respectively. It was obvious that the surface was deformed after photocatalytic treatment, but the polyhedral shape of LF particles was almost protected at pH 3. However, the particle size decreased to less than ~70 nm compared with the sole LF, and a slight agglomeration was evident due to RB5 degradation. As the pH value increased to pH 4, the morphology was significantly modified, and larger agglomerates

were observed. The average particle size was ~50 nm at pH 4, with a rougher surface. However, under the neutral experimental condition (pH 7.5), the particles of the sole LF consisting of agglomerates were mostly similar in shape and size (Figure S3d). The SEM image after 120 min irradiation under alkaline pH conditions (pH 10) is presented in Figure S3e. The particle sizes were in the ~50–80 nm range and the surfaces were covered with noticeable agglomeration, probably due to the RB5 molecules. Based on the EDAX results (Figure S3b–e), the major elements in LF and RB5 were La, Fe, and O, and C, N, and S, respectively. Their presence confirmed the interaction between LF and RB5 during the photocatalytic treatment process, and possibly adsorbed and/or mineralized RB5 residues on LF. The Fe content was ~21% for all different pH conditions. This value was slightly lower than that in the sole LF, indicating rather insignificant Fe (ferrous iron) leaching into the LF suspension. The second stage of SEM analysis features the effect of PS and multiple use on LF morphology. For comparative purposes, Figure S3a,b, which were already given in the previous experimental data set, are referred to here as Figure S4a,b, respectively. Upon PS addition, a considerable surface morphology change was observed, as is evident in Figure S4c. The texture is more wrinkled and composed of polyhedron- and deformed-shaped aggregate particles, with particle sizes that varied from ~45 nm to ~80 nm. The SEM images presented in Figure S4d,e indicated the morphological differences after four consecutive cycles. Changes were clearly noticed as undefined and irregular particles on the LF surface. Furthermore, a longer irradiation time after reuse influenced the common texture covered with undefined particles and aggregates on a large domain of the LF surface (Figure S4e). The EDAX spectra confirmed the existence of La, Fe, O, C, N, and S after four reuse cycles. Moreover, the Fe content retained practically stable. In general, pH adjustment did not exert a significant impact on the particle shape, while slight agglomerate formations were observed due to particle–particle interactions. However, the use of PS and reuse in four consecutive cycles appreciably affected the LF morphology.

The morphologies of LF and RB5 obtained at t = 0 (initial adsorption) and after photocatalytic treatment are presented in Figure S5. The difference between the polyhedral LF particles as observed in Figure S5a was that they were extensively covered with the adsorbed RB5 (Figure S5b). As the RB5 dye was an anionic dye, it expresses negative charge due to sulphonate groups ($pK_a \approx 2$), which would be present as negatively charged ions. The isoelectric point of LF was reported as pH 8.9; therefore, the LF surface would be predominantly positively charged at the working solution of pH 3 [14,15]. Therefore, the electrostatic attractions between RB5 and LF could be maximized in a highly acidic medium (pH 3), resulting in a coverage of the surface that changed the morphology of LF. The presence of C, N, and S elements in the EDAX spectrum (Figure S3b) approved the adsorption of RB5. Figure S5c,d show SEM images of RB5 on the LF surface, which was irradiated for 120 min and 210 min. Figure S5c shows a smoother surface compared with sole LF. Upon a long period of irradiation time, the morphology was almost similar to the LF surface, with aggregated particles due to the photocatalytic degradation of RB5 (Figure S5d). The adsorption of RB5 on LF particles in the presence of PS resulted in a nearly complete surface coverage compared with the extent of adsorption in the absence of PS (Figure S5e). The smoothly covered surface consisted of aggregated particles. Following photocatalytic degradation with PS for 120 min irradiation, the SEM image consisted of slightly deformed and smaller polyhedral-shaped LF particles with agglomeration (Figure S5f). The addition of PS in an acidic medium influenced the morphology and enhanced the degradation of RB5 adsorbed on LF. Generally speaking, the pH adjustment during photocatalysis did not exert a significant impact on particle shape, while slight agglomerate formations were observed. However, the use of PS and reusing catalyst for four consecutive cycles affected the morphology notably. The presence of La, O, and Fe amounts confirmed the reusability of LF and thereby its stability under the specified photocatalytic conditions.

3.4.3. FTIR Spectroscopy Analyses

Industrial dyes have a complicated chemical composition. Some dyes are very hydrophilic, whereas others easily adsorb/sorb onto surfaces and can co-exist with other chromophores and contaminants; therefore, the identification of organic dyes on (photo)catalytic materials can be a challenging task [30–36]. FTIR analysis was employed to examine the changes in RB5 functional groups as well as LF throughout the duration of photocatalysis [37–39]. FTIR bands associated with RB5 and LF were deduced from the literature findings and are presented in Table S1 [30,34,37,40]. The FTIR spectrum of untreated RB5 is presented in Figure S6a. The –N=N– azo chromophores of RB were represented by the band at 1487 $cm^{-1}$, and the S=O stretching vibration band located at 1049 $cm^{-1}$ belonged to the sulfonated group of its auxochrome. The main characteristic bands of RB5 at ~3512 $cm^{-1}$, 1342 $cm^{-1}$, and 1130 $cm^{-1}$ were attributed to N–H stretching in the amines, as well as the –C–O– and –CN groups of aromatic amines, respectively [25,30]. The band related to the $–CH_3$ asymmetric and symmetric vibrational stretching was located at 2989 $cm^{-1}$, while the $–CH_2$ asymmetric vibrational stretching band was detected at 2902 $cm^{-1}$ [31,32]. The three bands observed at 1001 $cm^{-1}$, 889 $cm^{-1}$, and 743 $cm^{-1}$ were all related to the =C–H groupings of the aromatic rings [29]. The phenyl groups of RB5 were represented by the bands in the range 740–690 $cm^{-1}$ [27]. The band at 1591 $cm^{-1}$ could be assigned to the C–C vibration of benzene [31]. The bands at 1410 $cm^{-1}$ and 1228 $cm^{-1}$ were ascribed to the stretching of aromatic C=C and amino C–N bonds, respectively [33]. The FTIR spectrum of LF is presented in Figure S6b. The broad band observed at 3189 $cm^{-1}$ was attributed to the characteristics of the H–O bending mode of absorbed water or the hydroxyl functional group. The bands at 2972 $cm^{-1}$ were assigned to the physically absorbed $CO_2$. The vibrations of the $CO_3^{2-}$ group were located at 1485 $cm^{-1}$, 1387 $cm^{-1}$, and 1068 $cm^{-1}$. The intense band at 534 $cm^{-1}$ was the main characteristic band of LF, corresponding to the stretching vibration of the Fe–O bond formed by the octahedral $FeO_6$ group in $LaFeO_3$. The weak band at 849 $cm^{-1}$ could also indicate Fe–O and O–Fe–O stretching bonds.

The effect of the initial (preliminary dark) adsorption of RB5 onto LF was also assessed by FTIR analysis. Figure S7 presents the spectrum of RB5 (20 mg/L), which was adsorbed on the LF (0.5 g/L) surface at pH 3 with/without the addition of 0.6 mM PS, and was recorded to vary between 15 and 20%. A slight shift in the bands was observed when PS (0.6 mM) was added at the t = 0 min condition. The bands at 3146 $cm^{-1}$ (O–H bending), 2978 $cm^{-1}$ ($CO_2$), 1483 $cm^{-1}$ ($CO_3^{2-}$ group), 812 $cm^{-1}$ (Fe–O and O–Fe–O stretching bonds), and 537 $cm^{-1}$ (Fe–O stretching) were related to LF, while the bands at 3446 $cm^{-1}$ (N–H stretching), 2978 $cm^{-1}$ ($–CH_3$ asymmetric and symmetric stretching), 2903 $cm^{-1}$ ($–CH_2$ asymmetric stretching), 1583 $cm^{-1}$ (C–C stretching in benzene), 1446 $cm^{-1}$ (aromatic C=C stretching), 1286 $cm^{-1}$ (–C–O– stretching), 1231 $cm^{-1}$ (C–N stretching), 1111 $cm^{-1}$ (the –C–N group of aromatic amines), 985 $cm^{-1}$, and 936 $cm^{-1}$ (=C–H group of aromatic rings) were associated with RB5 [26,30,34–40]. The band at 1045 $cm^{-1}$ could either correspond to the $CO_3^{2-}$ group of LF or the S=O stretching band of RB5. Compared with the RB5 spectrum, a new band appeared at 1629 $cm^{-1}$ [41]. This band could be related to the molecular water bending mode after the adsorption of RB5 on the LF surface.

The effect of pH on RB5 removal using LF was investigated in the pH range of 3–10 (LF = 0.5 g/L; RB5 = 20 mg/L), which was followed by FTIR analyses (Figure S6c). In all recorded spectra, the characteristic bands of both RB5 and LF were observed, as well as other vanishing and appearing bands. The band at 1487 $cm^{-1}$ representing the azo bond (–N=N–) of RB5 was cleaved and completely disappeared in the FTIR spectra obtained after 240 min photocatalytic treatment at pH 3. New bands were formed at 2858 $cm^{-1}$ and 1587 $cm^{-1}$, which correspond to $–CH_2$ bending and N–H bending, respectively. This observation could also indicate the generation of photocatalytic degradation products via the decolorization/cleavage of the azo bond followed by the disintegration of aromatic amines, even to dearomatization [31,42,43].

Moreover, the appearance of the band at 1386 $cm^{-1}$ indicated the presence of surface species with sulfone and/or sulfonate groups significant to RB5 degradation [26,30,40]. As

the pH increased to pH 4, the bands related to O–H bending and –$CH_2$ bending were still present. Complete decolorization of RB5 was not achieved since the band that belonged to the azo bond at 1500 $cm^{-1}$ was diminished; however, it still existed after 120 min photocatalytic treatment. There was no significant change in the spectra representing the photocatalytic degradation of neutral (pH 7.5) and alkaline (pH 10) media after 120 min. The broad band linked to the O–H bending appeared, and minor changes observed in other frequencies were not considerable. These observations were in accord with the results obtained for RB5 at pH > 4, namely that no photodegradation occurred for pH > 4.

The effect of PS addition to the photocatalytic treatment process on the functional groups was tested. Furthermore, the differences in the surface properties before and after four photocatalytic treatment cycles were assessed to explore the reuse potential of LF on decolorization efficiency, and respective results are presented in Figure S6d. Particularly for comparative purposes with the PS-added LF/UV-A treatment of RB5, the spectrum obtained at pH 3 displayed in Figure S6c was denoted as "without PS" in Figure S6d. The FTIR spectrum of the PS-added photocatalytic treatment system obtained after 120 min revealed the existence of a new and small band at 1480 $cm^{-1}$, which was related to the formation of $CO_3^{2-}$, while the band at 1221 $cm^{-1}$ corresponding to the amino C–N stretching vanished. The spectrum of the fourth reuse experiment obtained after 120 min treatment was almost similar to that of the original (first) LF/PS/UV-A experiment. However, the intensities of two bands related to the –$CH_3$ asymmetric and symmetric vibrational stretching (2989 $cm^{-1}$) and the –$CH_2$ asymmetric vibrational stretching (2912 $cm^{-1}$) were increased. In the spectrum obtained after 210 min photocatalytic treatment, the band at 1482 $cm^{-1}$ assigned to the $CO_3^{2-}$ group disappeared. Moreover, the intensities of the bands associated with the N–H stretching in amines (~3485 $cm^{-1}$), C–C stretching of benzene/N–H bending (~1585 $cm^{-1}$), and sulfone/sulfonate groups (~1392 $cm^{-1}$) significantly increased relative to those found after 210 min treatment, designating RB5 degradation [26]. In summary, the main differences were observed for the spectra obtained after photocatalytic treatment at pH 3 for the surface functional groups of RB5 and LF. The cleavage of the azo bond resulted from the decolorization of RB5 and the generation of possible degradation products. Especially $CO_3^{2-}$ formation was apparent for the conditions involving PS addition and the fourth cycle of the photocatalytic treatment system.

The progress of the photocatalytic reaction on the surface of LF coated with RB5 was also determined using FTIR spectroscopy for samples at different photocatalytic treatment times (120 min, 180 min, and 240 min) under an acidic medium at pH 3. The changes observed in FTIR spectra are shown in Figure S8. The band at 1487 $cm^{-1}$ representing the azo bond (–N=N–) of RB5 between benzene and naphthalene rings was shifted to a higher wavenumber (~1495 $cm^{-1}$) after 120 min and 180 min irradiation, while this band disappeared in the FTIR spectrum obtained after 240 min photocatalytic degradation. This result was consistent with the UV-vis absorbance decolorization spectra of RB5 represented in Figure S1. The new bands appeared at ~2860 $cm^{-1}$, ~1585 $cm^{-1}$, and ~1390 $cm^{-1}$, and they were related to the–$CH_2$ bending, N–H bending, and surface species, respectively, after 180 min and 240 min irradiation. However, the band at ~2860 $cm^{-1}$ was not observed in the spectrum of 120 min. In general, the bands at ~3500 $cm^{-1}$, ~1225 $cm^{-1}$, ~1140 $cm^{-1}$, and ~1045 $cm^{-1}$ corresponded to the N–H stretching in amines, amino C–N stretching, the C–N group of aromatic amines, and S=O stretching vibrations of RB5, respectively [26,35,38,39]. The characteristic bands of LF were also observed at ~840 $cm^{-1}$ (Fe–O and O–Fe–O stretching bonds) and ~530 $cm^{-1}$ (Fe–O stretching) [30,36,37,40,43]. It should also be indicated that the presence of a band at ~1487 $cm^{-1}$ signifying the main –N=N– group of azo chromophores present in the RB5 structure could also specify the presence of $CO_3^{2-}$ groups. Both assignments could reveal a system-specific dual indication of decolorization and mineralization efficiencies.

Under all reaction conditions, the observed FTIR bands were found to be in accordance with the expected degradation products of RB5 [31]. Moreover, FTIR results were

compatible with UV-vis spectroscopic data, proving the cleavage of RB5 chromophoric azo double bonds and degradation of aromatic parts during photocatalysis.

#### 3.4.4. Raman Spectroscopy Analyses

The Raman spectra of RB5, LF, and the spectral profiles obtained during LF-mediated photocatalysis are given for the range of 1800–400 $cm^{-1}$. The Raman spectrum of RB5 is displayed in Figure S9a. Raman band assignments are presented in Table S2. The vibrational assignment was reported on the basis of previous related work [44–46]. The most characteristic/prominent bands of RB5 at 511 $cm^{-1}$, 951 $cm^{-1}$, and 962 $cm^{-1}$; and 1157 $cm^{-1}$, 1300 $cm^{-1}$, and 1412 $cm^{-1}$, were attributed to the vibrations of naphthyl δCCC, naphthyl ρCH, aromatic βCH, aliphatic βCH, and νN = N groups, respectively. The strong band at 1547 $cm^{-1}$ and the shoulder at 1529 $cm^{-1}$ were assigned to the aromatic ring stretching vibrations of the phenyl (phenyl νCC) and naphtyl moieties (naphthyl νCC), respectively. The weak band at 1503 $cm^{-1}$ corresponded to the aromatic νCC and CN vibrations. The band at 1007 $cm^{-1}$ could be attributed to the ring breathing mode of the benzene rings. The observed band at 658 $cm^{-1}$ was associated with the $NH_2$ wagging mode, and the deformation modes of the same group were positioned in the 400–300 $cm^{-1}$ spectral range. The characteristic bands of the sulfonate group were located at 1223 $cm^{-1}$, 1190 $cm^{-1}$, and 1082 $cm^{-1}$, and corresponded to the stretching vibrations of the sulphate $–OSO_2O–$ group, while a weak band at 731 $cm^{-1}$ was assigned to the deformation of this group. The bands at 1366 $cm^{-1}$, 1040 $cm^{-1}$, and 555 $cm^{-1}$ were related to the sulphone $–SO_2–$ fragment of RB5. The bands at 1131 $cm^{-1}$ and 835 $cm^{-1}$ were attributed to the νCC alkane vibration and aliphatic νCC bond, respectively. The observed band at 449 $cm^{-1}$ could be assigned to the $–SO_2–$ moiety. Raman spectroscopy was also employed to determine the structure distortion and oxygen motion of LF, and the spectrum is displayed in Figure S9b. The bands at 442 $cm^{-1}$, 480 $cm^{-1}$, and 1163 $cm^{-1}$ were related to the one-phonon scattering, while those at 1296 $cm^{-1}$ were assigned to the two-phonon scattering of $O^{2-}$. The observed band at 609 $cm^{-1}$ corresponded to the two-phonon scattering or impurity scattering [47–49]. The bands observed at 1470 $cm^{-1}$ and 1390 $cm^{-1}$ could be due to some impurity scattering formed during treatment [48,50]. The spectral profile changes in LF and RB5 at different pH conditions (pH 3, 4, 7.5, and 10) and after photocatalytic treatment are presented in Figure S9c. In the spectrum recorded at pH 3, the bands at 1552 $cm^{-1}$ (phenyl νCC), 1531 $cm^{-1}$ (naphthyl νCC), 1501 $cm^{-1}$ (νCC and νCN), 1227 $cm^{-1}$ and 1097 $cm^{-1}$ (ν$–OSO_2O–$ group), 1146 $cm^{-1}$ (aromatic βCH), 976 $cm^{-1}$ and 959 $cm^{-1}$ (naphthyl ρCH), 845 $cm^{-1}$ (aliphatic νCC bond), 768 $cm^{-1}$ (deformation of $–OSO_2O–$ group), 671 $cm^{-1}$ ($NH_2$ wagging mode), 555 $cm^{-1}$ (ν$–SO_2–$), and 510 $cm^{-1}$ (naphthyl δCCC) were all related to RB5. The overall LF bands were observed at 1473 $cm^{-1}$ and 1389 $cm^{-1}$ (impurity scattering); 1290 $cm^{-1}$ (two-phonon scattering of $O^{2-}$); 1167 $cm^{-1}$, 486 $cm^{-1}$, and 443 $cm^{-1}$ (one phonon scattering); and 620 $cm^{-1}$ (two-phonon scattering or impurity scattering). The presence of naphthyl and aromatic groups could indicate the formation of aromatic degradation products of RB5. Moreover, the existence of a sulphate group could signify the degradation of the sulfonate grouping of RB5. Obviously, these peaks were drastically decreased under pH 4 and pH 7 conditions, and they also entirely disappeared at pH 10. Hence, this finding was compatible with the pH-dependent variations of RB5-removal efficiencies. In fact, under alkaline pH conditions (at pH 10), only the vibrations of LF at 1466 $cm^{-1}$, 1396 $cm^{-1}$, 1298 $cm^{-1}$, and 1161 $cm^{-1}$ were observed, while the other bands associated with RB5 and LF were present at a very low intensity or completely absent. It could be concluded that no detectable degradation products were formed after photocatalysis under the specified experimental conditions at pH 10. The effect of PS addition and multiple-reuse applications on the spectral profiles of RB5 and LF was investigated and is displayed in Figure S9d. After PS addition, the bands belonging to phenyl νCC, naphthyl νCC, νCC, CN, νN=N, aromatic βCH, naphthyl δCCC, and the deformation of the $–OSO_2O–$ groups vanished. These findings suggested the aromatic bond cleavage of RB5 into oxidation intermediates. Upon PS addition, all LF bands were present with slight shifts. After 120 min of photocatalytic

treatment during the multiple-reuse experiments, the sharpness and intensity of the bands decreased. The bands related to naphthyl νCC, νCC, νCN, naphthyl ρCH, aliphatic νCC bond, naphthyl δCCC moieties of RB were missing. Moreover, the band at 620 $cm^{-1}$ corresponding to the two-phonon scattering or impurity scattering of LF disappeared. In the spectrum belonging to the multiple-reuse application after 210 min of photocatalytic treatment, the absence of several bands related to the aromatic moieties of RB5 could indicate the presence of some aromatic degradation products in the reaction medium. The Raman profile changes in LF and RB5 after 120 min, 180 min, and 240 min of photocatalytic treatment at pH 3 are depicted in Figure S10. Upon 120 min irradiation, the bands at 1541 $cm^{-1}$ (phenyl νCC), 1522 $cm^{-1}$ (naphthyl νCC), 1514 $cm^{-1}$ (νCC, νCN), 1155 $cm^{-1}$ (aromatic βCH), 1238 $cm^{-1}$ and 1099 $cm^{-1}$ (ν–$OSO_2O$– group), 999 $cm^{-1}$ and 956 $cm^{-1}$ (naphthyl ρCH), 847 $cm^{-1}$ (aliphatic νCC bond), 775 $cm^{-1}$ (deformation of –$OSO_2O$ group), 681 $cm^{-1}$ ($NH_2$ wagging mode), 554 $cm^{-1}$ (ν–$SO_2$–), and 521 $cm^{-1}$ (naphthyl δCCC) were all related to RB5. The bands associated with LF were observed at 1472 $cm^{-1}$ and 1398 $cm^{-1}$ (impurity scattering); 1300 $cm^{-1}$ (two-phonon scattering of $O^{2-}$); 1155 $cm^{-1}$, 497 $cm^{-1}$, and 442 $cm^{-1}$ (one phonon scattering); and 646 $cm^{-1}$ (two-phonon scattering or impurity scattering) in accordance with previous findings [44–51]. These bands were observed with minor shifts in the Raman spectra obtained upon irradiation periods of 180 min and 240 min. The existence of naphthyl and aromatic groups could signify the generation of aromatic degradation products of RB5. The Raman spectra of RB5 adsorbed on LF at acidic medium (pH 3) exhibited the characteristic bands of both RB5 and LF (Figure S11). Comparing the spectra of RB5 and LF, a few spectral changes involving the band intensity variations and wavenumber shifts were apparent due to the surface interactions prevailing between LF and RB5. The bands at 1589 $cm^{-1}$ (phenyl νCC); 1540 $cm^{-1}$ (naphthyl νCC); 1528 $cm^{-1}$ (aromatic νCC, νCN); 1414 $cm^{-1}$ (νN=N); 1392 $cm^{-1}$, 1030 $cm^{-1}$, and 539 $cm^{-1}$ ($\nu SO_2$); 1349 $cm^{-1}$ (aliphatic βCH); 1224 $cm^{-1}$, 1180 $cm^{-1}$, and 1087 $cm^{-1}$ (ν(–$OSO_2O$–)); 1129 $cm^{-1}$ (νCC alkane); 977 $cm^{-1}$ and 960 $cm^{-1}$ (naphthyl ρCH); 830 $cm^{-1}$ (aliphatic νCC); 717 $cm^{-1}$ ($\delta OSO_2O$); 653 $cm^{-1}$ ($wNH_2$); and 539 $cm^{-1}$ (naphthyl δCCC) were related to RB5 [39–41]. The bands at 1492 $cm^{-1}$ and 1392 $cm^{-1}$ were assigned to the impurity scattering of LF. The characteristic bands of LF shifted to lower wavenumbers and were located at 1281 $cm^{-1}$ (two-phonon scattering of $O^{2-}$) and 595 $cm^{-1}$ (two-phonon scattering or impurity scattering). The other bands at 1154 $cm^{-1}$, 488 $cm^{-1}$, and 432 $cm^{-1}$ could be attributed to the one-phonon scattering of LF [44–51]. In the same manner, the bands appearing at 1154 $cm^{-1}$ and 432 $cm^{-1}$ might belong to the aromatic βCH and –$SO_2$– moieties of RB5, respectively. The wavenumbers of the bands related to both RB5 and LF shifted slightly in the presence of PS compared with sole LF/UV-A treatment. No remarkable change in RB5 due to adsorption on the LF surface was observed upon PS addition.

## 4. Conclusions and Recommendations

Lately, perovskite-type oxides with general-formula $ABO_3$ have received great attention because of their unique physicochemical properties, including photocatalytic activity under near-UV/visible light radiation. Previous work demonstrated that the semiconductor $LaFeO_3$ (lanthanum–iron oxide; abbreviated as LF herein) is capable of degrading refractory and/or toxic organic pollutants found in water and wastewater as a potential alternative to the more traditional heterogeneous semiconductor-type photocatalysts, such as titania. In this study, a home-made lanthanum–iron oxide (LF) was used for the photocatalytic and peroxydisulfate (PS)-enhanced photocatalytic treatment of the model industrial pollutant and commercially important model textile dye Reactive Black 5 (RB5). In this work, special emphasis was placed on the instrumental analyses of LF composition and surface morphology during and after LF/UV-A and LF/PS/UV-A treatments of hydrolyzed aqueous RB5. The experimental study revealed that an acidic pH (<4) and PS addition (0.6–1.2 mM) were critical in terms of efficient color and DOC removals. The addition of PS also improved the reuse performance of LF; hence, the multiple use of LF was possible with the LF/PS/UV-A

treatment process, with complete color and highly efficient DOC removals. A detailed assessment of changes in structural features, surface morphology, and chemical composition indicated that the photocatalyst surface was covered by noticeable agglomerates after the photocatalytic treatment of RB5. Based on the SEM/EDAX findings, the major elements after LF/UV-A treatment were identified as La, Fe, O, C, N, and S. The presence of these elements confirmed RB5 and its degradation/mineralization end-products being adsorbed on the LF surface. The Fe content of LF only slightly decreased after treatment, indicating that only some minor Fe ion leaching occurred into the reaction bulk. PS addition to the LF/UV-A treatment process on the other hand resulted in a considerable change in surface morphology (namely, a decrease in particle size, particle agglomeration, surface coverage, etc.). After multiple reuse cycles, undefined and irregular particles were principally noticed on the LF surface, indicating some modifications in the surface morphology. FTIR and Raman results were, generally speaking, comparable with the UV-vis spectroscopic data, confirming the effective cleavage of RB5 azo dye chromophores and the subsequent photocatalytic degradation of the aromatic moieties during LF-mediated, PS-enhanced heterogeneous photocatalysis.

**Supplementary Materials:** The following supporting information can be downloaded at: https://www.mdpi.com/article/10.3390/w15050906/s1, Figure S1. UV-vis absorbance spectra of RB5 before and during LF/UV-A treatment. Conditions: 20 mg/L RB5, pH3, 0.5 g/L LF, UV-A. Samples 1-9 indicate initial (t = 0 min), t = 5 min, 15 min, 30 min, 60 min, 120 min, 180 min, 210 min and 240 min conditions. Figure S2: Synchronous-scan fluorescence spectra of RB5. Conditions: 20 mg/L RB5, pH 3, 0.5 g/L LF, UV-A. Samples 1–9 indicate initial (t = 0 min), t = 5 min, 15 min, 30 min, 60 min, 120 min, 180 min, 210 min, 240 min conditions. Figure S3: SEM images (left) ×200,000, (right) ×100,000 and EDAX elemental analysis of (a) LF; (b) 0.5 g/L LF, pH 3, UV-A, 240 min; (c) 0.5 g/L LF, pH 4, UV-A, 120 min; (d) 0.5 g/L LF, pH 7.5, UV-A, 120 min; (e) 0.5 g/L LF, pH 10, UV-A, 120 min. Figure S4: SEM images (left) ×200,000, (right) ×100,000 and EDAX elemental analysis of (a) LF; (b) 0.5 g/L LF, pH 3, UV-A, 240 min; (c) 0.5 g/L LF, 0.6 mM PS, pH 3, UV-A, t = 120 min; (d) 0.5 g/L LF, 0.6 mM PS, pH 3, UV-A, t = 120 min, final/4th cycle; (e) 0.5 g/L LF, 0.6 mM PS, pH 3, UV-A, t = 210 min, final/4th cycle. Figure S5: SEM images (left) ×200,000, (right) ×100,000 and EDAX elemental analysis of (a) LF; (b) 0.5 g/L LF, pH 3, UV-A, t = 0 min; (c) 0.5 g/L LF, pH 3, UV-A, t = 120 min; (d) 0.5 g/L LF, pH 3, UV-A, t = 240 min; (e) 0.5 g/L LF, 0.6 mM PS, pH 3, UV-A, t = 0 min; (f) 0.5 g/L LF, 0.6 mM PS, pH 3, UV-A, t = 120 min. Figure S6: FTIR spectra of (a) RB5, (b) LF, (c) pH effect, (d) PS addition and reuse effect. Figure S7: FTIR spectra of RB5 adsorbed on LF (t = 0). Figure S8: FTIR spectra of LF coated with RB5 after 120 min, 180 min, and 240 min UV-A irradiation. Figure S9: Raman spectra of (a) RB5, (b) LF, (c) pH effect: (black) pH 3: 0.5 g/L LF, UV-A, 240 min; (red) pH 4, 0.5 g/L LF, UV-A, 120 min; (blue) pH 7.5, 0.5 g/L LF, UV-A, 120 min; 0.5 g/L LF; (green) pH 10, UV-A, 120 min; (d) PS addition and reuse effect: (black) without PS: 0.5 g/L LF, pH 3, UV-A, 240 min; (red) with PS: 0.5 g/L LF, 0.6 mM PS, pH 3, UV-A, t = 120 min; (blue) 120 min: 0.5 g/L LF, 0.6 mM PS, pH 3, UV-A, t = 120 min, final/4th cycle; (green) 210 min 0.5 g/L LF, 0.6 mM PS, pH 3, UV-A, t = 210 min, final/4th cycle. Figure S10: Raman spectra of LF coated with RB5 after 120 min, 180 min, and 240 min UV-A irradiation. Figure S11: Raman spectra of RB5 adsorbed on LF (t = 0). Table S1: FTIR spectral bands of RB5 and LF. Table S2: Raman spectral bands of RB5 and LF.

**Author Contributions:** Conceptualization, I.A.-A. and M.B.; methodology, I.A.-A., M.B., O.K.-U. and N.T.; software, O.K.-U. and N.T.; validation, O.K.-U. and N.T.; formal analysis, I.A.-A. and M.B.; investigation, I.A.-A., M.B., O.K.-U. and N.T.; resources, I.A.-A., M.B. and N.T.; data curation, I.A.-A., O.K.-U., M.B. and N.T.; writing, I.A.-A., M.B. and N.T.; visualization, I.A.-A., M.B., O.K.-U. and N.T.; supervision, I.N.S.; project administration, I.A.-A. and M.B.; funding acquisition, I.A.-A., M.B. and N.T. All authors have read and agreed to the published version of the manuscript.

**Funding:** This research was funded by the Istanbul Technical University, grant number MAB-2021–43188 (Olga Koba-Ucun).

**Institutional Review Board Statement:** Not applicable.

**Data Availability Statement:** Data is available upon request.

**Acknowledgments:** This work was supported by the Istanbul Technical University under Project MAB-2021–43188. The authors are thankful to Eksoy Chemicals for the gift reactive dye sample.

**Conflicts of Interest:** The authors declare no conflict of interest.

## References

1. Shore, J. Cellulosics Dyeing. In *The Society of Dyers and Colorists*; Alden Press: Oxford, UK, 1995.
2. Freeman, H.S.; Reife, A. Dyes, Environmental Chemistry. In *Kirk-Othmer Encyclopedia of Chemical Technology*; John Wiley & Sons, Inc.: Hoboken, NJ, USA, 2003; pp. 431–463.
3. Lucas, M.S.; Peres, J.A. Degradation of Reactive Black 5 by Fenton/UV-C and ferrioxalate/$H_2O_2$/solar light processes. *Dyes Pigment.* **2007**, *7*, 622–629.
4. Bilinska, L.; Gmurek, M.; Ledakowicz, S. Comparison between industrial and simulated textile wastewater treatment by AOPs-biodegradability, toxicity and cost assessment. *Chem. Eng. J.* **2016**, *306*, 550–559.
5. Armaković, S.J.; Savanović, M.M.; Armaković, S. Titanium dioxide as the most used photocatalyst for water purification: An overview. *Catalysts* **2023**, *13*, 26. [CrossRef]
6. Chen, X.; Wang, W.; Xiao, H.; Hong, C.; Zhu, F.; Yao, Y.; Xue, Z. Accelerated $TiO_2$ photocatalytic degradation of Acid Orange 7 under visible light mediated by peroxymonosulfate. *Chem. Eng. J.* **2012**, *193–194*, 290–295.
7. Samy, M.; Kumi, A.G.; Salama, E.; ElKady, M.; Mensah, K.; Shokry, H. Heterogeneous activation of persulfate by a novel nano-magnetite/ZnO/activated carbon nanohybrid for carbofuran degradation: Toxicity assessment, water matrices, degradation mechanism and radical and non-radical pathways. *Process Saf. Environ. Prot.* **2023**, *169*, 337–351.
8. Wang, X.; Chen, Z.; He, Y.; Yi, H.; Zhang, C.; Zhou, Q.; Xiang, X.; Gao, Y.; Huang, M. Activation of persulfate-based advanced oxidation processes by 1T-$MoS_2$ for the degradation of imidacloprid: Performance and mechanism. *Chem. Eng. J.* **2023**, *451*, 138575. [CrossRef]
9. Azouzi, W.; Sigle, W.; Labrim, H.; Benaissa, M. Sol-gel synthesis of nanoporous $LaFeO_3$ powders for solar applications. *Mater. Sci. Semicond. Process.* **2019**, *104*, 104682. [CrossRef]
10. Mokoen, M.; Koao, L.F.; Dejene, B.F.; Tshabalala, K.G.; Motloung, S.J. Structure, morphology, and optical properties of lanthanide orthovanadate powders prepared by chemical bath deposition. *Mater. Today Commun.* **2023**, *34*, 105001. [CrossRef]
11. Zurlo, F.; Di Bartolomeo, E.; D'Epifanio, A.; Felice, V.; Sora, I.N.; Tortora, L.; Licoccia, S. $La_{0.8}Sr_{0.2}Fe_{0.8}Cu_{0.2}O_{3-\delta}$ as "cobalt-free" cathode for $La_{0.8}Sr_{0.2}Ga_{0.8}Mg_{0.2}O_{3-\delta}$ electrolyte. *J. Power Source* **2014**, *271*, 187–194. [CrossRef]
12. Parrino, F.; García-López, E.; Marcì, G.; Palmisano, L.; Felice, V.; Sora, I.N.; Armelao, L. Cu-substituted lanthanum ferrite perovskites: Preparation, characterization and photocatalytic activity in gas-solid regime under simulated solar light irradiation. *J. Alloys Compd.* **2016**, *682*, 686–694. [CrossRef]
13. Natali Sora, I.; Fumagalli, D. Fast photocatalytic degradation of pharmaceutical micropollutants and ecotoxicological effects. *Environ. Sci. Pollut. Res.* **2017**, *24*, 12556–12561.
14. Birben, N.C.; Lale, E.; Pelosato, R.; Turkten, N.; Sora, I.N.; Bekbolet, M. Photocatalytic bactericidal performance of $LaFeO_3$ under solar light in the presence of natural organic matter: Spectroscopic and mechanistic evaluation. *Water* **2021**, *13*, 2785. [CrossRef]
15. Birben, N.C.; Lale, E.; Pelosato, R.; Uyguner Demirel, C.S.; Natali Sora, I.; Bekbolet, M. Photocatalytic bactericidal performance of $LaFeO_3$ under solar light: Kinetics, spectroscopic and mechanistic evaluation. *Water* **2021**, *13*, 1135. [CrossRef]
16. Turkten, N.; Natali Sora, I.; Tomruk, A.; Bekbolet, M. Photocatalytic degradation of humic acids using $LaFeO_3$. *Catalysts* **2018**, *8*, 630. [CrossRef]
17. Koba-Ucun, O.; Arslan-Alaton, I.; Sora, I.N.; Bekbölet, M. Persulfate-enhanced lanthanum iron oxide-mediated photocatalysis can effectively degrade an aqueous industrial dye and mineralize water and wastewater. *Desalin. Water Treat.* **2022**, *267*, 215–230. [CrossRef]
18. Arslan-Alaton, I.; Akmehmet-Balcioglu, I. Photochemical and heterogeneous photocatalytic degradation of waste vinylsulphone dyes: A case study with hydrolyzed Reactive Black 5. *J. Photochem. Photobiol. A Chem.* **2001**, *141*, 247–254. [CrossRef]
19. Arslan-Alaton, I.; Karatas, A.; Pehlivan, O.; Koba-Ucun, O.; Olmez-Hanci, T. Effect of UV-A-assisted iron-based and UV-C-driven oxidation processes on organic matter and antibiotic resistance removal in tertiary treated urban wastewater. *Catal. Today* **2020**, *361*, 152–158. [CrossRef]
20. Wan, K.; Li, Y.; Wang, Y.; Wei, G. Recent advance in the fabrication of 2D and 3D metal carbides-based nanomaterials for energy and environmental applications. *Nanomaterials* **2021**, *11*, 246. [CrossRef]
21. Wan, K.; Liu, C.; Wang, Y.; Zhang, W.; Qi, P.; Guo, L.; Wei, G.; Liu, X. Recent advances in the synthesis and regulation of 3D metal carbide-based hybrid architectures for water environmental remediation and monitoring. *J. Environ. Chem. Eng.* **2022**, *10*, 108994. [CrossRef]
22. Wan, K.; Wang, Y.; Liu, C.; Wei, C.; Lv, S.; Tang, X.; Fang, T.; Zhao, J.; Wei, G.; Qi, P.; et al. Facile synthesis of hierarchical $Ti_3C_2$@FeOOH nanocomposites for antimony contaminated wastewater treatment: Performance, mechanisms, reutilization, and sustainability. *Chem. Eng. J.* **2022**, *450*, 138038. [CrossRef]
23. Badvi, K.; Javanbakht, V. Enhanced photocatalytic degradation of dye contaminants with $TiO_2$ immobilized on ZSM-5 zeolite modified with nickel nanoparticles. *J. Clean. Prod.* **2021**, *280*, 124518. [CrossRef]

24. Chen, J.; Xiong, Y.; Duan, M.; Xiang, L.; Li, J.; Fang, S.; Qin, S.; Zhang, R. Insight into the Synergistic Effect of adsorption–photocatalysis for the removal of organic dye pollutants by Cr-Doped ZnO. *Langmuir* **2020**, *36*, 520–533. [CrossRef] [PubMed]
25. Lau, Y.-Y.; Wong, Y.-S.; Ong, S.-A.; Ho, L.-N.; Hussin, K.; Lutpi, N.A. Intermolecular mechanistic treatment of recalcitrant environmental pollutants: Azo, benzene, naphthalene and vinyl sulfone. *J. Taiwan Inst. Chem. Eng.* **2017**, *76*, 27–34. [CrossRef]
26. Saroyan, H.; Ntagiou, D.; Rekos, K.; Deliyanni, E. Reactive Black 5 degradation on manganese oxides supported on sodium hydroxide modified graphene oxide. *Appl. Sci.* **2019**, *9*, 2167. [CrossRef]
27. Zhang, Q.; Xie, X.; Liu, Y.; Zheng, X.; Wang, Y.; Cong, J.; Yu, C.; Liu, N.; He, Z.; Liu, J.; et al. Sugar sources as co-substrates promoting the degradation of refractory dye: A comparative study. *Ecotoxicol. Environ. Saf.* **2019**, *184*, 109613. [CrossRef]
28. Chen, Y.; D'Errico, G.; Fabbricino, M.; Gallucci, N.; Pontoni, L.; Race, M.; Yao, S. Role of organic nanoparticles on transport and fate of various dyes in aqueous solution. *Environ. Res.* **2022**, *215*, 114179. [CrossRef]
29. Uyguner-Demirel, C.S.; Turkten, N.; Kaya, D.; Bekbolet, M. Effect of oxidative and non-oxidative conditions on molecular size fractionation of humic acids: $TiO_2$ and Cu-doped $TiO_2$ photocatalysis. *Environ. Sci. Pollut. Res.* **2022**, *29*, 85413–85432. [CrossRef]
30. Kale, R.D.; Kane, P.B. Synthesis of PVP stabilized bimetallic nanoparticles for removal of azo based reactive dye from aqueous solution. *Sustain. Chem. Pharm.* **2018**, *10*, 153–162. [CrossRef]
31. Bilal, M.; Rasheed, T.; Iqbal, H.M.N.; Hu, H.; Wang, W.; Zhang, X. Toxicological assessment and UV/$TiO_2$-based induced degradation profile of Reactive Black 5 dye. *Environ. Manag.* **2018**, *61*, 171–180. [CrossRef]
32. Neoh, C.H.; Lam, C.Y.; Lim, C.K.; Yahya, A.; Bay, H.H.; Ibrahim, Z.; Noor, Z.Z. Biodecolorization of recalcitrant dye as the sole sourceof nutrition using *Curvularia clavata* $NZ_2$ and decolorization ability of its crude enzymes. *Environ. Sci. Pollut. Res.* **2015**, *22*, 11669–11678. [CrossRef]
33. Ziane, S.; Bessaha, F.; Marouf-Khelifa, K.; Khelifa, A. Single and binary adsorption of reactive black 5 and Congo red on modified dolomite: Performance and mechanism. *J. Mol. Liq.* **2018**, *249*, 1245–1253. [CrossRef]
34. Gosavi, P.V.; Biniwale, R.B. Pure phase $LaFeO_3$ perovskite with improved surface area synthesized using different routes and its characterization. *Mater. Chem. Phys.* **2010**, *119*, 324–329. [CrossRef]
35. Li, S.; Jing, L.; Fu, W.; Yang, L.; Xin, B.; Fu, H. Photoinduced charge property of nanosized perovskite-type $LaFeO_3$ and its relationships with photocatalytic activity under visible irradiation. *Mater. Res. Bull.* **2007**, *42*, 203–212. [CrossRef]
36. Thirumalairajan, S.; Girija, K.; Ganesh, I.; Mangalaraj, D.; Viswanathan, C.; Balamurugan, A.; Ponpandian, N. Controlled synthesis of perovskite $LaFeO_3$ microsphere composed of nanoparticles via self-assembly process and their associated photocatalytic activity. *Chem. Eng. J.* **2012**, *209*, 420–428. [CrossRef]
37. Yahya, N.; Aziz, F.; Jaafar, J.; Lau, W.J.; Yusof, N.; Salleh, W.N.W.; Ismail, A.F.; Aziz, M. Impacts of annealing temperature on morphological, optical and photocatalytic properties of gel-combustion-derived $LaFeO_3$ nanoparticles. *Arab. J. Sci. Eng.* **2021**, *46*, 6153–6165. [CrossRef]
38. Abazari, R.; Sanati, S.; Saghatforoush, L.A. A unique and facile preparation of lanthanum ferrite nanoparticles in emulsion nanoreactors: Morphology, structure, and efficient photocatalysis. *Mater. Sci. Semicond. Process.* **2014**, *25*, 301–306. [CrossRef]
39. Abdallah, F.B.; Benali, A.; Triki, M.; Dhahri, E.; Nomenyo, K.; Lerondel, G. Investigation of structural, morphological, optical and electrical properties of double-doping Lanthanum ferrite. *J. Mater. Sci. Mater. Electron.* **2019**, *30*, 349–3358. [CrossRef]
40. Kale, R.D.; Kane, P.B. Decolourization by PVP stabilized Fe-Ni nanoparticles of Reactive Black 5 dye. *J. Environ. Chem. Eng.* **2018**, *6*, 5961–5969. [CrossRef]
41. Wawrzyniak, B.; Morawski, A.W. Solar-light-induced photocatalytic decomposition of two azo dyes on new $TiO_2$ photocatalyst containing nitrogen. *Appl. Catal.* **2006**, *62*, 150–158. [CrossRef]
42. Santos, P.B.; Dos Santos, H.F.; Andrade, G.F. Photodegradation mechanism of the RB5 dye: A theoretical and spectroscopic study. *J. Photochem. Photobiol. A Chem.* **2021**, *416*, 113315. [CrossRef]
43. Turkten, N.; Cinar, Z. Photocatalytic decolorization of azo dyes on $TiO_2$: Prediction of mechanism via conceptual DFT. *Catal. Today* **2017**, *287*, 169–175.
44. Lin-Vien, D.; Colthup, N.B.; Fateley, W.G.; Grasselli, J.G. *The Handbook of Infrared and Raman Characteristic Frequencies of Organic Molecules*; Academic Press: San Diego, CA, USA, 1991.
45. Aguayo, T.; Garrido, C.; Clavijo, R.E.; Gómez-Jeria, J.S.; Araya Monasterio, C.; Icaza, M.; Espinoza Moraga, F.; Campos Vallette, M.M. Raman and surface enhanced Raman scattering of a black dyed silk. *J. Raman Spectrosc.* **2013**, *44*, 1238–1245. [CrossRef]
46. Santos, P.B.; Santos, J.J.; Corrêa, C.C.; Corio, P.; Andrade, G.F.S. Plasmonic photodegradation of textile dye Reactive Black 5 under visible light: A vibrational and electronic study. *J. Photochem. Photobiol. A Chem.* **2019**, *371*, 159–165. [CrossRef]
47. Popa, M.; Frantti, J.; Kakihana, M. Lanthanum ferrite $LaFeO_{3+d}$ nanopowders obtained by the polymerizable complex method. *Solid State Ion.* **2002**, *154–155*, 437–445. [CrossRef]
48. Sierra Gallego, G.; Marín Alzate, N.; Arnache, O. A novel $LaFeO_{3-X}N_X$ oxynitride. Synthesis and characterization. *J. Alloys Compd.* **2013**, *549*, 163–169. [CrossRef]
49. Sharma, N.; Sharma, S.K.; Sachdev, K. Effect of precursors on the morphology and surface area of $LaFeO_3$. *Ceram. Int.* **2019**, *45*, 7217–7225. [CrossRef]

50. Lee, W.-Y.; Yun, H.J.; Yoon, J.-W. Characterization and magnetic properties of $LaFeO_3$ nanofibers synthesized by electrospinning. *J. Alloys Compd.* **2014**, *583*, 320–324. [CrossRef]
51. Mohammadi, M.; Sabbaghi, S.; Sadeghi, H.; Zerafat, M.M.; Pooladi, R. Preparation and characterization of $TiO_2$/ZnO/CuO nanocomposite and application for phenol removal from wastewaters. *Desalin. Water Treat.* **2016**, *57*, 799–809. [CrossRef]